PAPER

Molecular beam epitaxy of PtSe₂ using a codeposition approach

To cite this article: Maria Hilse et al 2022 2D Mater. 9 025029

View the <u>article online</u> for updates and enhancements.

You may also like

- High carrier mobility in single-crystal PtSe₂ grown by molecular beam epitaxy on ZnO(0001)
 Frédéric Bonell, Alain Marty, Céline
- Frédéric Bonell, Alain Marty, Céline Vergnaud et al.
- Interfacial electronic properties of 2D/3D (PtSe₂/CsPbX₃) perovskite heterostructure Xiang Xiang Feng, Biao Liu, Mengqiu Long et al.
- Engineering the magnetic properties of PtSe₂ monolayer through transition metal doping

doping Moumita Kar, Ritabrata Sarkar, Sougata Pal et al.

2D Materials



RECEIVED
21 November 2021

21 November 202

REVISED 22 March 2022

ACCEPTED FOR PUBLICATION

23 March 2022

PUBLISHED 5 April 2022

PAPER

Molecular beam epitaxy of PtSe₂ using a co-deposition approach

Maria Hilse^{1,*}, Ke Wang¹ and Roman Engel-Herbert^{2,3,4,5,*}

- Materials Research Institute, The Pennsylvania State University, University Park, PA 16802, United States of America
- Department of Materials Science and Engineering, The Pennsylvania State University, University Park, PA 16802, United States of America
- Department of Physics, The Pennsylvania State University, University Park, PA 16802, United States of America
- Department of Chemistry, The Pennsylvania State University, University Park, PA 16802, United States of America
- ⁵ Current address: Paul-Drude Institut für Festkörperelektronik, Leibniz-Institut im Forschungsverbund Berlin e.V., Berlin 10117, Germany
- * Authors to whom any correspondence should be addressed.

E-mail: mxh752@psu.edu and engel-herbert@pdi-berlin.de

Keywords: chalcogenide materials, PtSe2, MBE

Abstract

The structural properties of co-deposited ultrathin PtSe₂ films grown at low temperatures by molecular beam epitaxy on c-plane Al₂O₃ are studied. By simultaneously supplying a Se flux from a Knudsen cell and Pt atoms from an electron-beam evaporator, crystalline (001)-oriented PtSe₂ films were formed between 200 °C and 300 °C. The long separation between substrate and electron beam evaporator of about 60 cm ensured minimal thermal load. At optimum deposition temperatures, a ten times or even higher supply rate of Se compared to Pt ensured that the pronounced volatility of the Se was compensated and the PtSe₂ phase was formed and stabilized at the growth front. Postgrowth anneals under a Se flux was found to dramatically improve the crystalline quality of the films. Even before the postgrowth anneal in Se, the crystallinity of PtSe₂ films grown with the co-deposition method was superior to films realized by thermal assisted conversion. Postgrowth annealed films showed Raman modes with narrower peaks and more than twice the intensity. Transmission electron microscopy investigations revealed that the deposited material transitioned to a two-dimensional layered structure only after the postgrowth anneal. PtSe₂ growth was found to start as single layer islands that preferentially nucleated at atomic steps of the substrate and progressed in a layer-by-layer like fashion. A close to ideal wetting behavior resulted in coalesced PtSe₂ films after depositing about 1.5 PtSe₂ layers. Detailed Raman investigation of the observed PtSe2 layer breathing modes of films grown under optimized co-deposition conditions revealed an interlayer coupling force constant of $5.0-5.6 \times 10^{19} \text{ N m}^{-3}$.

1. Introduction

Due to the promising electronic properties of the transition metal dichalcogenide (TMD) PtSe₂, such as carrier mobilities up to 1000 cm² V s⁻¹ and a scalable band gap from zero in the bulk up to 1.2 eV in the single layer (L)—comprising one monolayer (ML) of Pt sandwiched between two MLs of Se—limit, combined with its robustness in ambient conditions, PtSe₂ stands out among the recently proposed TMD candidates such as MoS₂ or WS₂, and makes it a potential contender as channel materials for low power high performance transistors [1–3]. First experimental work using exfoliated PtSe₂ flakes of 2 nm thickness amounting to 3 or 4

layers already demonstrated electron mobilities of 210 cm² V⁻¹s⁻¹ at room temperature in a field effect transistor configuration, which already outperforms other TMDs that range at or below 100 cm² V⁻¹ s⁻¹ [1, 3, 4]. These encouraging initial result were subsequently confirmed on exfoliated 2–3 nm thick PtSe₂ flakes [5, 6]. Excellent low-resistance ohmic contacts were achieved by keeping a sufficiently large PtSe₂ thickness in the source/drain region, and reducing it to few layers in the channel region [2, 3, 5]. Beyond those properties, PtSe₂ has also shown promise for photovoltaic [7], optoelectronic [8–15], and gas sensing applications [16], motivating the development of a scalable, low-temperature fabrication process yielding high-quality PtSe₂ layers

that can be easily integrated with existing material platforms.

The before mentioned exfoliation method is done at room temperature and therefore qualifies as a complementary metal-oxide-semiconductor (CMOS) back-end-of-line (BEOL) compatible process. However, exfoliation poses the risk of unintentional defect formation through mechanical stress and process environment, inherits limitations in thickness control, and additional roadblocks towards scaling up [3, 17], alternative methods suitable for bottom-up wafer-scale high-quality PtSe2 film synthesis with controlled layer thickness have to be found. Reports of PtSe2 synthesized by chemical vapor transport (CVT) failed similarly in the ability for up-scaling, and the lack of thickness control [3, 17]. Chemical vapor deposition has shown limited potential due to lack of thickness control, combined with a low degree of crystallinity and synthesis temperatures exceeding the BEOL process compatible threshold temperature of 450 °C [17-22]. The search for alternatives turned attention to thermal assisted conversion (TAC) of Pt layers into PtSe₂ in Se-saturated atmosphere. This method has been shown to be compatible with CMOS BEOL processes, but only few layer PtSe₂ were formed that showed a low degree of crystal ordering [2, 15, 17, 18, 23-27]. The inferior quality of PtSe₂ produced by TAC coincided with the observation of hole dominated transport [23, 27–30]. First-principle calculations have identified Pt vacancies as possible origin, which shift the Fermi level down towards the PtSe2 valence band through localized state formation in the bandgap [27]. Growth of TMDs such as MoSe₂, TiSe₂, HfSe₂, and WSe₂ by molecular beam epitaxy (MBE) has been shown to give significant material quality improvements [31–34]. As reported earlier, a TAC-like process solely performed in an MBE system revealed similar limitations as found for the conventional TAC method. However, a codeposition growth approach by simultaneously supplying Pt and Se fluxes and direct PtSe2 phase formation on the substrate proved itself successful on an epitaxial bilayer graphene/6 H-SiC(0001) substrate [18]. This process was performed at 270 °C, involving a post-growth annealing step to 400 °C, both compatible with CMOS BEOL fabrication. Furthermore, angle-resolved photoemission spectroscopy did not show signs of localized defect states due to impurities or defects in the band gap down to the single layer limit. MBE thus offers the potential to produce high-quality PtSe₂. A stringent determination of the electronic properties and possible application in electronic devices calls for an investigation and optimization of PtSe₂ growth on insulating, atomically flat and even amorphous substrates.

This work aims at a comprehensive investigation of PtSe₂ growth on crystalline Al₂O₃(0001) using a co-deposition growth approach in MBE. First, the

effect of substrate temperature on the degree of crystallinity in PtSe₂ is evaluated by growing 10 nm thick films in a temperature range from 100 °C to 500 °C. Characterization of the sample topography by atomic force microscopy (AFM), and crystal properties by reflection high-energy electron diffraction (RHEED), x-ray diffraction (XRD), and Raman spectroscopy identified an optimum growth temperature in the range between 200 °C and 300 °C. Subsequently, the excess Se FR relative to the Pt flux was determined to be ≥10. RHEED, AFM, XRD, Raman, and transmission electron microscopy (TEM) revealed a consistent improvement of the crystallinity for 20- and 2-layer thick samples that were subject to a post-growth anneal in a Se flux at 400 °C for 30 min. By employing the optimized growth procedure, PtSe2 films with varying thickness from below one single layer up to 20 layers were grown. The growth was observed to nucleate at the substrate step edges of the Al₂O₃. Full coverage of the substrate with a coalesced PtSe2 film was obtained after nominally depositing 1.5 L, proving a close to ideal wetting behavior and a pronounced lateral growth from initially nucleated PtSe2 islands. The interlayer breathing force constant for the lowfrequency out-of-plane interlayer vibration observed in Raman for the 1-5 L thick PtSe2 films was calculated to range from 5.0 to $5.6 \times 10^{19} \,\mathrm{N}\,\mathrm{m}^{-3}$, coinciding with values reported in literature for Bi₂Se₃, PtS₂, and PtSe₂, and indicating strong interlayer interaction in PtSe₂ [3, 35, 36].

Utilizing optimized growth conditions, 3 L thick PtSe₂ films were grown on back-gated MOSFET structures using Si/SiO₂ wafers with buried Al gates and an amorphous Al₂O₃ gate oxide grown by ALD, that yielded record on/off ratios for PtSe₂ channel MOSFET devices [37].

1.1. Methods

1.1.1 Growth

Single crystal c-plane Al_2O_3 substrates (Cryscore, 0.2° miscut towards the a-plane) with terrace steps running along the $11\bar{2}0$ direction were cleaned with acetone, isopropyl alcohol, and DI-water using an ultrasonic bath of 3 min for each step. To condition the sapphire surface, substrates were annealed for 8 h at 1150 °C in air and subsequently cleaned in acetone, isopropyl alcohol, and DI-water using a 15 min ultrasonic bath for each step. Finally, substrate pieces were dipped into Nanostrip for 40 min at 140 °C and rinsed thoroughly with DI-water.

MBE growth was carried out in a R450 type MBE reactor (DCA Instruments) with a base pressure of 3×10^{-10} Torr. Pt was supplied using an ultra-high vacuum linear four-pocket electron beam evaporator source (Telemark model 575-02) operated at 10 kV with emission currents of about 120 mA, which produced a flux of about 1.5 \times 10¹³ atoms cm⁻² s⁻¹ measured at the sample position using a quartz crystal microbalance from Colnatec. The tooling factor for Pt

2D Mater. **9** (2022) 025029 M Hilse et al

fluxes was determined from physical film thicknesses in XRD and TEM. The evaporator was situated 60 cm below the substrate to minimize the thermal load during growth. During a 30 min long Pt deposition with an emission current of about 190 mA (Pt flux $\sim 2 \times 10^{14}$ atoms cm $^{-2}$ s $^{-1}$) the unheated substrate remained at constant temperature of 10 °C. Selenium was supplied from a low temperature Knudsen effusion cell operated at about 150 °C, resulting in a flux of about 2×10^{14} atoms cm $^{-2}$ s $^{-1}$.

1.1.2. AFM

Ex-situ investigation of the film and substrate surface topography was performed using a Dimension Icon Bruker Atomic Force Microscope operated in Peak-Force Tapping mode using RTESPA type AFM tips from Bruker and a scan rate of about 1 Hz.

1.1.3. Raman spectroscopy

Raman spectra were recorded ex-situ with a Horiba LabRam system using a laser power of 110 mW and a wavelength of 532 nm. A neutral density power filter of 10% or 5% was typically used with a notch filter of $\pm 10~\rm cm^{-1}$. Laser light was focused onto the sample through an objective lens (magnification $100\times$) and collected for 30 and 120 s in a backscattering geometry using an 1800 g mm $^{-1}$ grating. An autofocus routine was carried out in the spectral range of the E_g PtSe $_2$ Raman mode between 150 and 200 cm $^{-1}$ before taking data. Measurement height was set to the z-position of maximum signal during the autofocus routine. All spectra were normalized to the 417 cm $^{-1}$ mode of the Al $_2$ O $_3$ substrate.

1.1.4. XRD

A four-circle diffractometer (Panalytical X'Pert³) equipped with a PIXcel 3D detector was used for ex-situ XRD measurements. Cu $K_{\alpha 1}$ radiation was focused on the sample in high resolution configuration.

1.1.5. Transmission electron microscopy

Cross-sectional transmission electron microscope (TEM) specimen were fibbed using a FEI Helios 660 focused ion beam (FIB) system. A 1 kV final cleaning step was applied after samples became electron transparent to avoid ion beam damage to the sample surface during FIB. The high angle annular dark field scanning transmission electron microscopy (STEM) was performed using a FEI aberration corrected S/TEM at 200 kV (Titan G2 60-300) and energy-dispersive spectroscopic (EDS) maps were collected in STEM mode using a SuperX EDS system (Bruker).

2. Effect of deposition temperature

A series of nominally (based on the earlier described Pt flux calibration) 10 nm thick PtSe₂ films were grown on c-plane sapphire at varying temperatures between 100 °C and 500 °C. A Se to Pt FR of 10 was used at all temperatures to ensure sufficient Se oversupply. Figure 1 shows RHEED images in the upper left collected from the substrate along the $11\bar{2}0$ direction with high contrast including sharply defined Kikuchi lines as expected for an ultra-flat and clean substrate. The surface AFM topography of the substrate in the bottom left shows nearly perfect atomic step terrace morphology with a root mean square (rms) roughness of 0.08 nm.

For PtSe₂ films grown at 100 °C the pronounced highly intense RHEED pattern from the sapphire substrate transitioned into a diffuse, evenly distributed intensity, typical for amorphous material. The film topography revealed an ultra-flat surface with a root mean square (rms) value of 0.36 nm absent of any distinct topographic feature typical for dense, amorphous films. No PtSe₂ related diffraction peaks were observed in the XRD $2\theta-\omega$ scans, see figure 2.

At higher growth temperatures of 200 °C and 300 °C broad diffraction rods appeared in RHEED, marked by yellow lines in figure 1. The distance between the diffraction rods were in good agreement with the in-plane reciprocal spacing expected for PtSe2. In addition, two broad Laue rings were found in RHEED for films grown at 200 °C, indicated by yellow circle segments, indicating a polycrystallinity or at least a poor in-plane alignment of PtSe2. Diffraction rod intensity was more pronounced for films grown at higher temperature while the Laue rings appeared weaker in intensity, indicating a higher degree of crystallinity and an improved in-plane alignment. The surface roughness is comparable for films grown in this temperature regime and was found to be somewhat higher compared to 100 °C. The surface texture consisted of a dense array of small islands. As the degree of crystallinity improved at 300 °C, islands were found to be larger and exhibit smooth surfaces in AFM. This evolution can also be seen in XRD presented in figure 2, where a PtSe₂(001) diffraction peak appears at $2\theta = 16.7^{\circ}$ only at 200 °C, which had increased intensity for films grown at 300 °C.

Even higher growth temperatures lead to a different spacing in the RHEED diffraction rods, highlighted by light blue lines in figure 1, which corresponded to the lattice spacing of pure Pt. Marked by light blue circle segments, a minimum of 5 Laue rings was observed. At the highest temperature, Pt crystallinity appeared more ordered and therefore the Laue rings had reduced intensity. The Pt formation at these temperatures lead to an increased island density and height, resulting in a higher surface roughness. In accordance with RHEED, XRD characterization in figure 2 showed solely a Pt(111) peak at $2\theta = 39.7^{\circ}$ at high temperature, i.e. no signature of the desired PtSe₂ formation was present. The sample temperature was therefore too high for the given Se flux to get incorporated into the solid phase of PtSe₂.

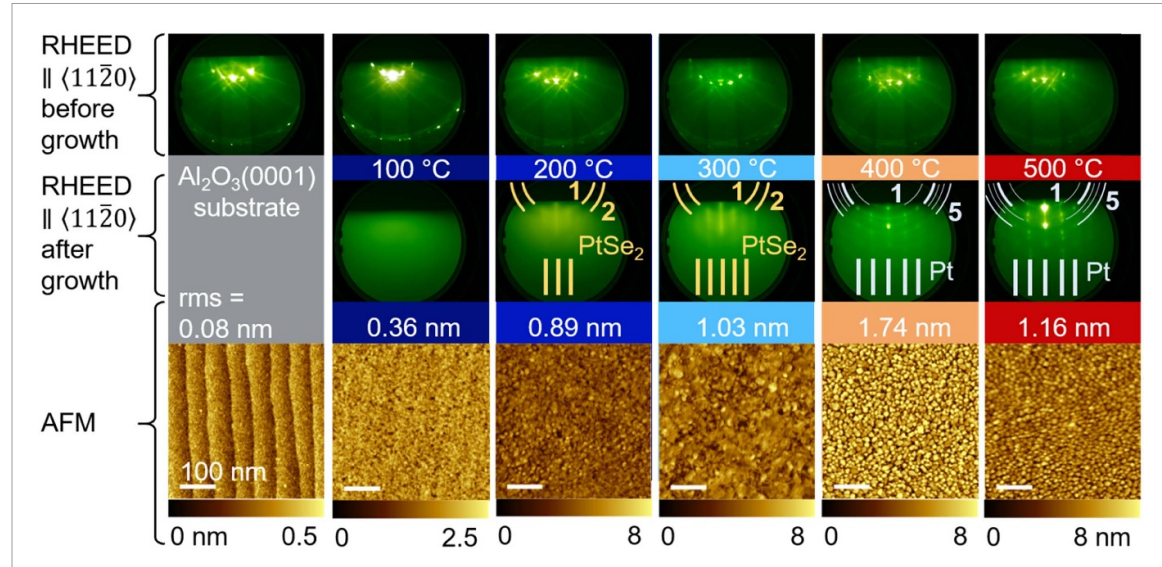


Figure 1. RHEED and AFM data collected from the pristine sapphire substrate and 10 nm thick PtSe₂ films grown at different temperatures. Yellow lines and circles in RHEED denote the position of PtSe₂ diffraction rods and Laue rings, light blue lines and circles indicate Pt related diffraction rods and Laue circles. The root mean square (rms) roughness values are given above the AFM micrographs. The lateral dimensions of all AFM images are in the scale of 100 nm, their respective *z*-height scale is given below each image.

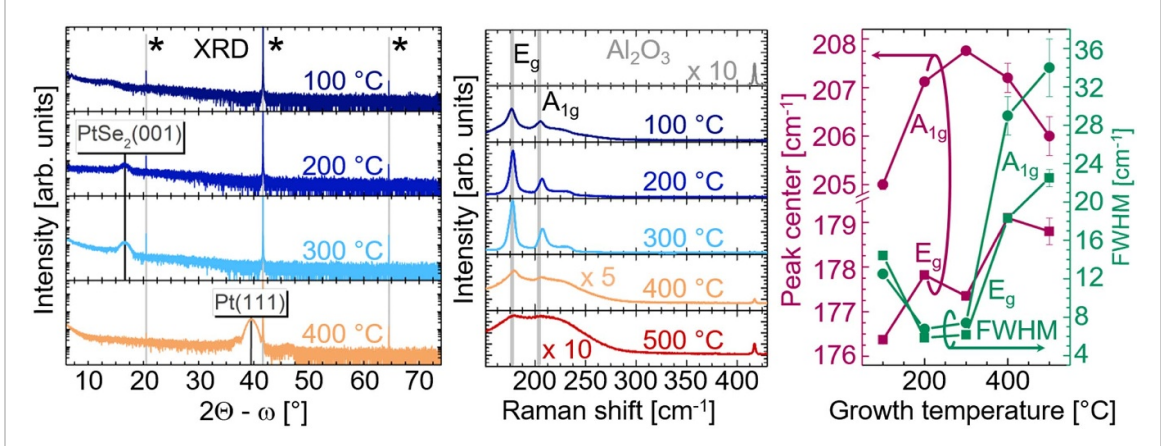


Figure 2. $2\theta - \omega$ XRD and Raman data corresponding to the samples shown in figure 1. * labeled XRD peaks correspond to diffractions from Al₂O₃. Right plot shows the FWHM and peak center of the E_g and A_{1g} modes versus the growth temperature.

The middle panel in figure 2 shows Raman spectra obtained from the PtSe₂ films introduced in figure 1 along with the bare sapphire substrate at the top for comparison. The most pronounced substrate feature was a weak Raman peak at 417 cm⁻¹ from the pristine Al₂O₃ [38]. Two additional modes at 178 and 206 cm⁻¹ were found in the Raman spectra for samples grown at 100 °C, attributed to the $E_{\rm g}$ and $A_{\rm lg}$ mode of PtSe2 respectively. Both modes became more pronounced in intensity and sharper with increasing growth temperature up to 300 °C, while a broad shoulder developed at around 230 cm⁻¹ attributed to overlapping LO modes in PtSe₂ [29, 39]. There is a slight peak shift observed with increasing temperature for the A_{1g} and E_g peak, as summarized on the right in figure 2, accompanied by a significant drop in the full width at half maximum (FWHM) of both modes, and an increase in the A_{1g} to E_{g} intensity

ratio from 0.38 at 100 °C to 0.52 at 300 °C. Positions of the vibrational modes are consistent with earlier reports on PtSe₂ [24, 39]. As the A_{1g} mode is related to the out-of-plane vibration mode in PtSe2, the increase of the A_{1g} to E_g intensity ratio was found to be indicative of an improvement in long range crystalline order of the film [24, 29], a trend also revealed in the FWHM values [40]. Raman results are thus in excellent agreement with XRD and AFM data, indicating that the highest quality PtSe₂ films were achieved at growth temperature between 200 °C and 300 °C. Although, PtSe₂ related vibration modes were still observed at higher temperatures, peak intensities were significantly decreased and FWHM values increased. The E_g mode shifted slightly to higher wave numbers for films grown at 400 °C-500 °C, which is consistent with a decreasing thickness of PtSe₂. Meanwhile, the A_{1g} mode shifted back to 206 cm⁻¹

in this temperature window indicating a declining long range crystalline order. Both trends are in good agreement with the observation that PtSe₂ formation at these temperatures is neglectable. No vibration modes from pure Pt films were expected in the recorded range. It is therefore concluded that although the structural characterization of RHEED and XRD indicated that elemental Pt was the dominant phase, still small amounts of PtSe₂ were nevertheless present [3, 18, 24, 29, 30].

3. Necessary Se oversupply

About 10 nm thick films were deposited at 200 °C with varying Se/Pt FRs from 2 to 20 to study the amount of Se excess flux necessary for PtSe₂ phase formation in the optimum growth temperature window. Figure 3 shows RHEED, AFM, and Raman analysis of the FR series.

RHEED images of films grown at a FR of 2 and 5 showed hazy background intensity characteristic for amorphous material. A smooth surface with large, circularly shaped islands with an average distance of 100–400 nm was observed for FR = 2, while at FR = 5 the surface was characterized by an uniform and dense island array, having a three times larger rms roughness value. The PtSe2 related Raman modes were weak for FR = 2, indicating that $PtSe_2$ formation was hindered, which became stronger and narrower at FR = 5. Broad diffraction rods and Laue rings from PtSe₂ appeared for FRs larger than 5. Samples grown with high FR showed an island textured surface with slightly increased rms values at higher FR. Peak intensities of the Eg and Alg Raman modes showed a consistent increase with FR. Similarly, the FWHM of associated peaks decreased compared to FR = 5 and stayed nearly constant for FRs of 10-20.

Therefore, optimal FR values were found to be in the range of 10-15 with the smallest rms roughness values at FR = 10, and smallest Raman FWHM values at FR = 15, both giving a good compromise between degree of crystallinity and surface roughness.

4. Effect of post-growth anneal

Earlier work on co-deposition growth of PtSe₂ and conversion of pure Pt layers into PtSe₂ by direct selenization showed that film crystallinity significantly improved through a post-growth anneal in Se atmosphere [18, 41]. Figure 4 shows the effect of an *in-situ* post-growth anneal for 30 min of a 10 nm thick PtSe₂ film grown at 200 °C with FR larger than 10.

RHEED showed much more pronounced diffraction rods of PtSe₂ after the post-growth anneal and Laue rings were not present anymore. Specifically, 3rd and 4th order diffraction rods were observed after the anneal (highlighted by yellow lines), indicating a significant improvement of the long-range crystalline order in the film. While the in-plane alignment was

much improved the width of the RHEED streaks was also reduced, indicating a larger grain size and thus overall an improved crystallinity. Although the rms roughness of the film increased slightly (0.89 nm and 1.33 nm for a 10 nm thick film grown at 200 °C before and after the post-growth anneal, respectively), film surface topography showed less spherically shaped islands after the anneal. Instead irregularly shaped grains with a lateral size of 20-50 nm were found, confirming the RHEED trends and directly revealing the formation of larger grains during the postgrowth anneal. XRD measurements are in agreement with these findings. The PtSe₂ 001 peak intensity at $2\theta = 17.1^{\circ}$ increased by more than a factor of 2. In addition, higher order diffraction peaks, such as the PtSe₂ 003 diffraction at $2\theta = 54^{\circ}$ were detected after the post-growth annealing step.

The improved crystallinity after the post-growth anneal was also reflected in Raman, where $E_{\rm g}$ and $A_{\rm 1g}$ modes had a higher intensity. The intensity ratio $A_{\rm 1g}$ over $E_{\rm g}$ increased from 0.39 to 0.7, while the peak widths were reduced by 0.7 cm⁻¹ and 0.3 cm⁻¹ for the $E_{\rm g}$ and $A_{\rm 1g}$ mode, respectively.

A post-growth annealing step in Se atmosphere was thus key to improve the film crystallinity. It has to be noted that the highest quality PtSe₂ films were obtained using the two-step approach, where films were deposited at lower temperatures between 200 °C to 300 °C and annealed at 400 °C during a post-growth anneal under a Se flux, whereas direct growth at 400 °C (figures 1 and 2) did not yield similarly high-quality material, although the exact same Se fluxes were supplied. Furthermore, post-growth selenization anneals resulted in noticeable improvements within the first 20 min irrespective of PtSe₂ film thickness.

The dramatic post-growth annealing effect on the crystallinity and long range order of PtSe₂ was seen best in cross-sectional STEM images shown in figure 5. Few layer deposition of PtSe₂ at 200 °C resulted in disconnected 2 nm thick PtSe₂ islands. No layered or otherwise crystalline order could be observed within the individual islands. This was attributed to a low degree of crystallinity as well as insufficient drive for an in-plane alignment.

After a 30 min postgrowth anneal at 400 °C in Se atmosphere the disjointed islands had transformed into a continuous 2 L, i.e. 1 nm thick PtSe₂ film. Although a portion of approximately ¾ of the PtSe₂ film is not showing a distinct epitaxial relation, ¼ of the top right layer encircled in figure 5 is. In this part a coherent crystal ordering in the PtSe₂ coinciding with the zone axis of the substrate can be seen in the high-resolution STEM with a lateral size of about 10 nm. The post-growth anneal therefore not only is crucial for the two-dimensional structure to evolve but furthermore increases the crystal ordering within the individual PtSe₂ layers as well. An estimate of the PtSe₂ crystalline domain sizes in optimized samples of

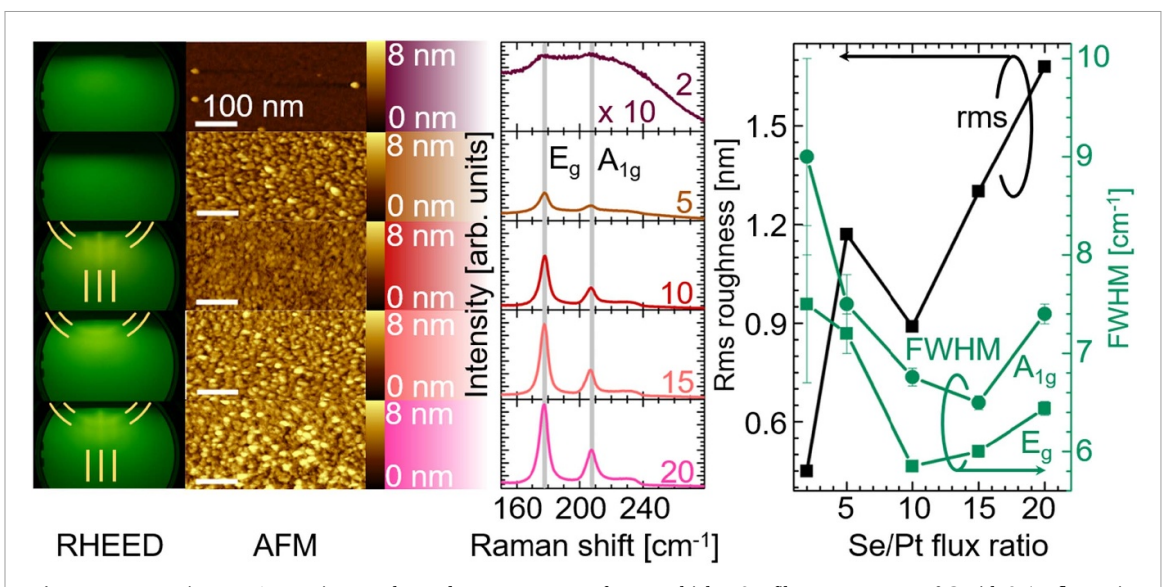


Figure 3. RHEED images, AFM micrographs, and Raman spectra of 10 nm-thick PtSe₂ films grown at 200 $^{\circ}$ C with Se/Pt flux ratio from top to bottom of 2, 5, 10, 15, and 20. Right plot shows the FWHM of the $E_{\rm g}$ and $A_{\rm 1g}$ modes as well as the rms roughness. For ease of comparison, the RHEED, AFM, and Raman data for the sample grown at a flux ratio of 10 from figures 1 and 2 is included.

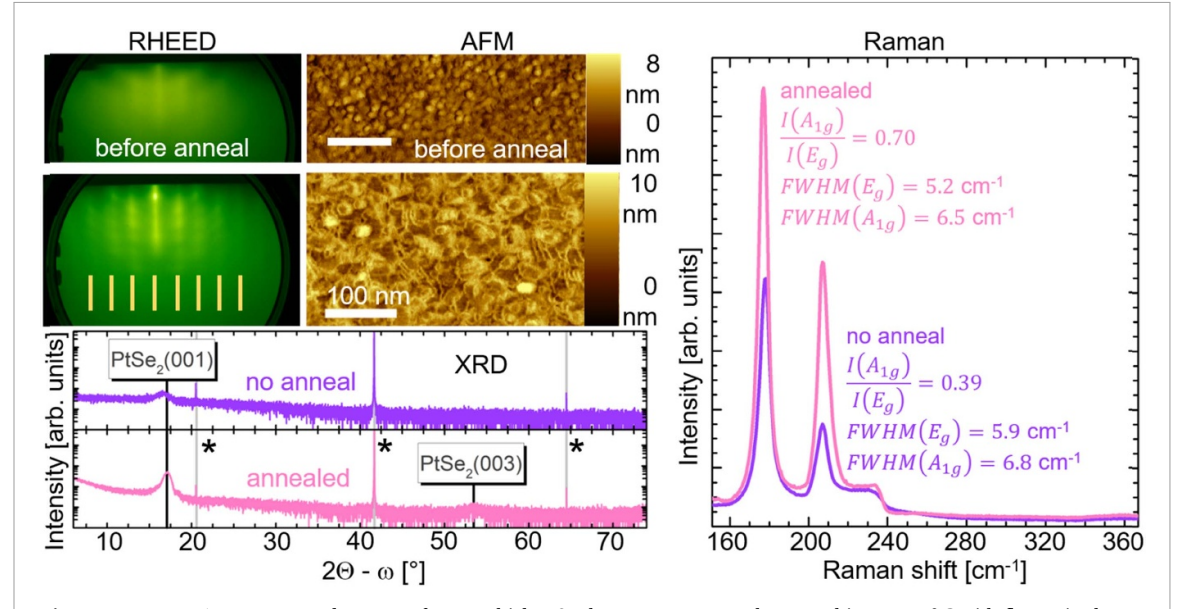


Figure 4. RHEED, AFM, XRD, and Raman of 10 nm thick PtSe₂ layers grown on ε -plane sapphire at 200 °C with flux ratios larger than 10 and annealed at 400 °C for 30 min in Se after growth. Diffraction rods from PtSe₂ are highlighted by yellow lines in RHEED. The RHEED, AFM, XRD, and the Raman spectra of an unannealed film grown under identical conditions from figures 1 and 2 are included for comparison. * labeled XRD peaks correspond to diffractions from Al₂O₃.

10 nm to 50 nm can be derived from AFM in figure 4 and TEM in figure 5.

5. Down-scaling of the film thickness

Using the optimized growth conditions of a deposition temperature of 200 $^{\circ}$ C, a Se/Pt FR larger than 10 and Se postgrowth anneal for 30 min to 400 $^{\circ}$ C, a PtSe₂ thickness series ranging from nominally one single layer up to 20 layers was grown.

Figure 6 shows an AFM micrograph of the sub-L sample, illustrating the nearly perfect atomic terrace substrate surface. The height profile from A to B across a terrace edge revealed a step height of (2.7 ± 0.9) Å, while an PtSe₂ island step height of (5.0 ± 0.9) Å was extracted from the line scan between C and D. While the first height difference is in good agreement with the interplanar distance of 2.17 Å found for $\{0001\}$ Al₂O₃, the PtSe₂ island height is in excellent agreement with the interplanar distance of PtSe₂ $\{001\}$. The PtSe₂ islands formed on sapphire have thus a thickness of one single layer, and the majority of islands appear to touch the substrate surface step edges. Either PtSe₂ preferentially nucleated at step edges and subsequently grew laterally over the terraces, or step edges are not preferential nucleation

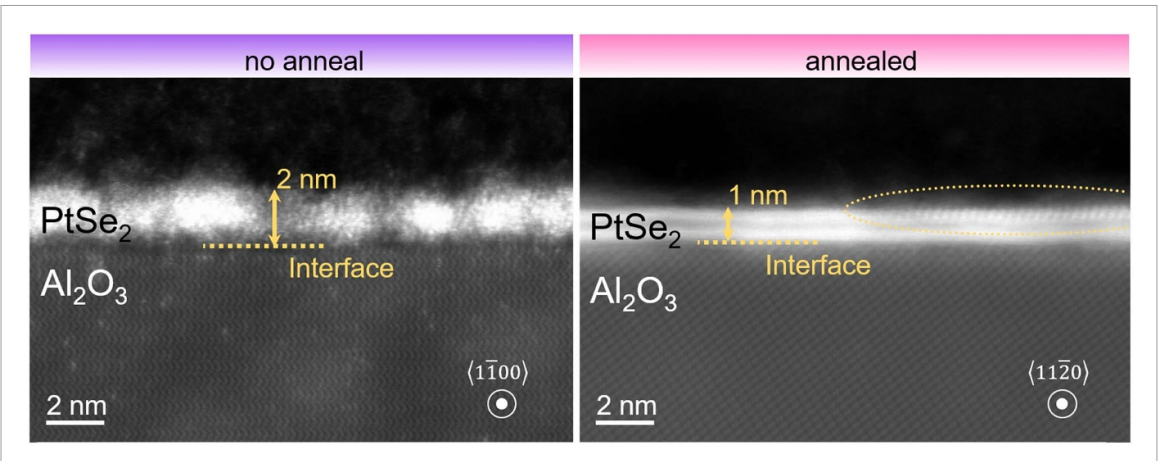


Figure 5. High-resolution STEM of a 2 L-thick PtSe₂ layer grown on $Al_2O_3(0001)$ after growth at 200 °C (left—image taken along the $1\bar{1}00$ -zone axis), and after a followed Se post-growth anneal (right—image taken along the $11\bar{2}0$ -zone axis).

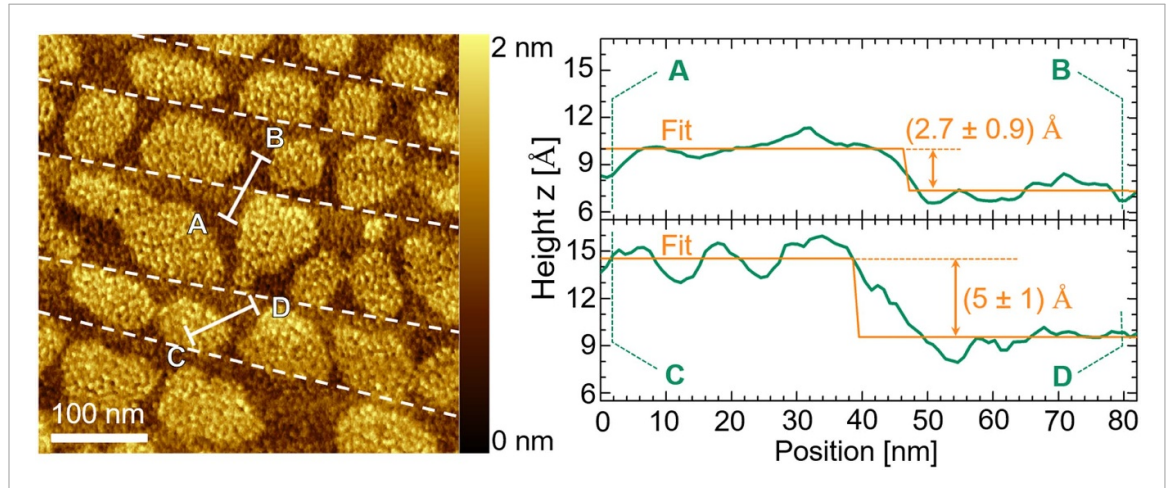


Figure 6. AFM micrograph of a sub-L $PtSe_2$ film grown on c-plane sapphire at 200 °C. Extracted line profiles from A to B across the substrate step edges—traced for better visibility by dashed lines, and C to D across the edge of a $PtSe_2$ island along with a step function fit is shown on the right.

sites, but represent a sizeable Schwoebel barrier that cannot be overcome at this low temperature. It is noticable that PtSe₂ has the tendency to grow in a layer-by-layer fashion and therefore exhibited very good wetting behavior on sapphire. No bilayer nucleation was observed in AFM scans for this sample. The excellent wetting behavior was further supported by RHEED observation, where the sapphire diffraction pattern completely vanished after the deposition of nominally 1.5 PtSe₂ layers. This remarkable result indicates that PtSe₂ can be scaled down to a single layer and that coalesced films are to be expected in the single layer limit.

Figure 7 shows AFM micrographs and Raman spectra of the PtSe₂ thickness series.

For the 1 and 2 L deposition, the film covered the substrate uniformly. The underlying sapphire step terrace structure was still visible in the AFM scans. Three-layer-PtSe₂ and thicker films developed a grainy texture, the average step height between grains remained to be about a single PtSe₂ layer thickness. Films of 3 L thickness and above show

the characteristic surface texture of spherical shaped islands on smooth patches of material.

In addition to the E_g and A_{1g} modes at 160 and 240 cm⁻¹, respectively Raman spectra were extended to smaller energies closer to the laser line. 1 L PtSe₂ showed very weak Raman signal, only one distinct Eg peak was detected, which shifted to smaller wave numbers with increasing layer number. In contrast, no noticeable peak shift was found for the A_{1g} mode. For films consisting of more than a single layer, an interlayer vibration mode (LVM) around 24 cm⁻¹ evolved which shifted to smaller energies with increasing layer number, until it could not be distinguished from the main laser line at a film thickness of 6 PtSe₂ layers. The nature of this mode was deduced from polarization dependent Raman scattering to be a layer breathing mode [3, 35]. Additional LVMs occurred in the ultra-low frequency range for even thicker films starting at 3 L thick films but could not be resolved individually. Instead a broad intensity band up to 40 cm⁻¹ was seen in Raman for thicker films [39].

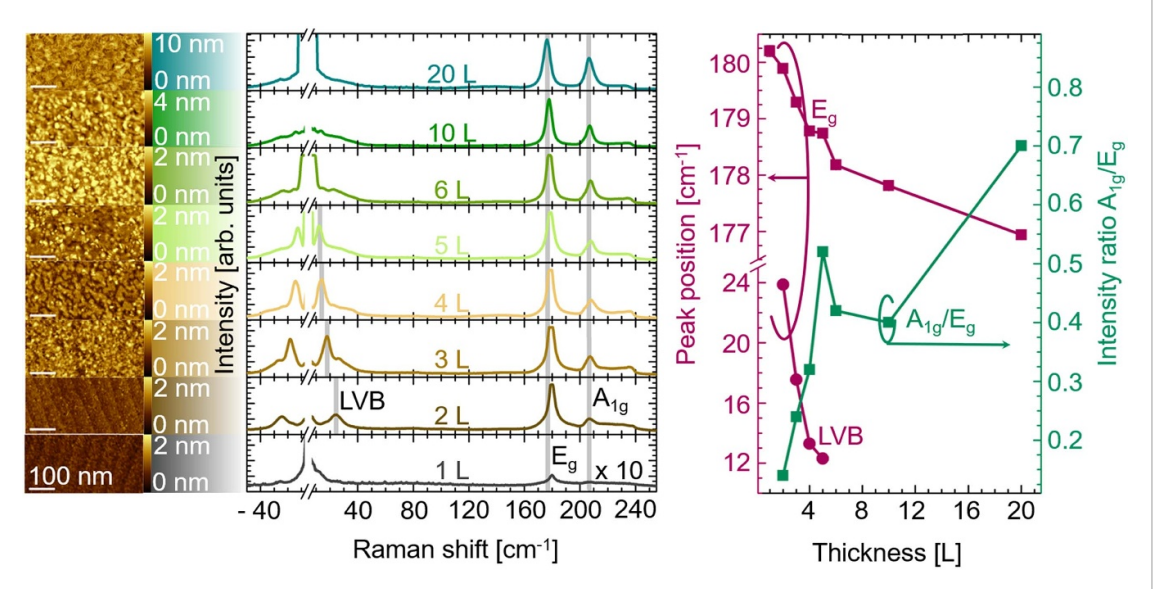


Figure 7. AFM micrographs and Raman spectra including ultra-low frequency modes collected from PtSe₂ films grown on $Al_2O_3(0001)$ at 200 °C followed by a post-growth Se anneal at 400 °C for 30 min. The Raman intensity for the 1 L sample is scaled by a factor of 10 as indicated.

To demonstrate the observed peak shifts for the LVM and Eg mode, Raman peaks were fitted and the extracted peak position and intensity ratio A_{1g}/E_g plotted versus the layer thickness in figure 7. The trend of E_g and LVM peak shift with increasing thickness is in good agreement with previously published results [3, 18, 24, 29, 30]. The LVM for the 2 L film $(\omega(2))$ was found at 23.87 cm⁻¹ and a fit to the LVM dependence on N = number of layers for the first $N_0 = 1$ phonon branch $(\omega(N) = \omega(2) \sqrt{1 - \cos(\frac{N_0 \pi}{N})})$ in figure 7 yielded 25.2 cm⁻¹. Calculations of the interlayer coupling force constant K^{\perp} for these values of $\omega(2)$ following $\omega(2) = \frac{1}{\sqrt{2\pi}c} \sqrt{\frac{K^{\perp}}{M}}$ with c = speed of light, and M = mass of one PtSe₂ layer per unit area resulted in $K^{\perp} = 5.0 \times 10^{19} \,\mathrm{N} \,\mathrm{m}^{-3}$, and $K^{\perp} = 5.6 \times 10^{19} \,\mathrm{N} \,\mathrm{m}^{-3}$, respectively [36]. Similar values for the interlayer breathing force constant are reported for Bi₂Se₃, and PtS₂, and overlap with published values on PtSe₂, confirming a strong interlayer interaction in PtSe2 [3, 35]. The intensity ratio A_{1g}/E_g showed a consistent increase with layer thickness from values less than 0.2 up to 0.7 for the 20 L thick PtSe₂ film, similar to the trend observed for the samples in figure 4 with and without post-growth Se anneal. This observation is most likely linked to the out-of-plane vibration nature of the A_{1g} mode (In this mode the Se atoms in the upper ML are displaced homogeneously out-ofplane against the Se atoms in the lower ML within one L of PtSe2.), which shows a consistent intensity increase with increasing film thickness throughout literature [18, 24]. The intensity ratio A_{1g}/E_g is therefore a sensitive indicator for the crystallinity and thickness of the material.

6. Conclusion

This work evaluates the microstructural properties of MBE grown PtSe2 films using a co-deposition synthesis method. In contrast to TAC, where only one to few-layer PtSe₂ films were realized on top of a thicker, metallic Pt layer [2, 41], this approach enabled the deposition of PtSe₂ films directly on insulating Al₂O₃ substrates with excellent film thickness control ranging from 1 to 20 layers, which showed remarkably high crystalline quality compared to any previous bottom-up growth attempts. Charcterization by AFM, RHEED, XRD, and Raman spectroscopy identified an optimum growth temperature range between 200 and 300 °C with an excess Se FR relative to the Pt flux of ≥ 10 . A remarkable improvement of the crystallinity for 20- and 2-layer thick samples was observed after PtSe₂ films were subjected to a postgrowth anneal for 30 min in a Se flux at 400 °C. STEM revealed that the two-dimensional layered texture of PtSe2 was only realized after such a post-growth anneal. Crystalline PtSe2 grain sizes ranged between 10 nm and 50 nm. PtSe₂ co-deposition growth was observed to nucleate at the substrate step edges. A close to ideal wetting behavior and a pronounced lateral growth lead to a full coverage of the substrate with a coalesced PtSe₂ film after nominally depositing 1.5 L. A strong interlayer interaction in PtSe2 coinciding with values reported for Bi₂Se₃, PtS₂, and PtSe₂ was observed by an interlayer breathing force constant ranging from 5.0 to 5.6 \times 10¹⁹ N m⁻³ for the lowfrequency out-of-plane interlayer vibration mode in Raman for the 1–5 L thick PtSe₂ films [3, 35, 36].

Despite the fact that optimized reported growth conditions yielded crystalline domain sizes that were

only on the order of 10 nm to 50 nm, 3 L thick PtSe₂ films grown on back-gated MOSFET structures using Si/SiO₂ wafers with buried Al gates and an amorphous Al₂O₃ gate oxide grown by ALD, showed record on/off ratios for PtSe2 channel MOSFET devices [37]. These encouraging results will motivate further work to improve the crystalline properties of PtSe₂. Although carrier mobilities of PtSe₂ films codeposited under optimized MBE growth conditions ranged in the single digit $cm^2 V^{-1} s^{-1}$ [37], the demonstrated improvement of long-range crystalline order in the material caused by a simple annealing procedure in Se atmosphere provides a roadmap towards increasing crystalline domain sizes and thus further enhance carrier mobilities. Our work has demonstrated that the upper limit of Se supply accessible in MBE, which was used for the post-growth anneal, is not sufficient to compensate the Se desorption out of the co-deposited PtSe₂ film at temperatures higher than 400 °C [41]. To push crystalline domain sizes well beyond lateral sizes of 50 nm, an ex-situ CVT annealing after MBE co-deposition growth and *in-situ* Se anneal at higher temperatures under significantly higher Se background pressures seems very likely to succeed but is beyond the scope of this work.

Data availability statement

All data that support the findings of this study are included within the article (and any supplementary files).

Acknowledgments

Work of the presented paper has been facilitated by The Pennsylvania State University Two-Dimensional Crystal Consortium—Materials Innovation Platform (2DCC-MIP), which is supported by NSF cooperative Agreements Nos. DMR-1539916 and DMR-2039351.

ORCID iD

Maria Hilse https://orcid.org/0000-0002-2824-1549

References

- [1] Zhang W, Huang Z, Zhang W and Li Y 2014 Two-dimensional semiconductors with possible high room temperature mobility *Nano Res.* 7 1731–7
- [2] Wang Y et al 2015 Monolayer PtSe₂, a new semiconducting transition-metal-dichalcogenide, epitaxially grown by direct selenization of Pt Nano Lett. 15 4013–8
- [3] Zhao Y et al 2017 High-electron-mobility and air-stable 2D layered PtSe₂ FETs Adv. Mater. 29 1604230
- [4] Wang F Q, Zhang S, Yu J and Wang Q 2015 Thermoelectric properties of single-layered SnSe sheet Nanoscale 7 15962–70
- [5] Yang Y, Jang S K, Choi H, Xu J and Lee S 2019 Homogeneous platinum diselenide metal/semiconductor coplanar structure fabricated by selective thickness control *Nanoscale* 11 21068–73

- [6] Ciarrocchi A, Avsar A, Ovchinnikov D and Kis A 2018 Thickness-modulated metal-to-semiconductor transformation in a transition metal dichalcogenide *Nat. Commun.* 9 919
- [7] Wang L, Li J J, Fan Q, Huang Z F, Lu Y C, Xie C, Wu C-Y and Luo L-B 2019 A high-performance near-infrared light photovoltaic detector based on a multilayered PtSe₂/Ge heterojunction J. Mater. Chem. C 7 5019–27
- [8] Deng S, Li L and Zhang Y 2018 Strain modulated electronic, mechanical, and optical properties of the monolayer PdS 2, PdSe 2, and PtSe₂ for tunable devices ACS Appl. Nano Mater. 1 1932–9
- [9] Zhang W, Guo H T, Jiang J, Tao Q C, Song X J, Li H and Huang J 2016 Magnetism and magnetocrystalline anisotropy in single-layer PtSe₂: interplay between strain and vacancy J. Appl. Phys. 120 013904
- [10] Avsar A, Ciarrocchi A, Pizzochero M, Unuchek D, Yazyev O V and Kis A 2019 Defect induced, layer-modulated magnetism in ultrathin metallic PtSe₂ Nat. Nanotechnol. 14 674–8
- [11] Manchanda P, Enders A, Sellmyer D J and Skomski R 2016 Hydrogen-induced ferromagnetism in two-dimensional Pt dichalcogenides *Phys. Rev.* B 94 104426
- [12] Kar M, Sarkar R, Pal S and Sarkar P 2019 Engineering the magnetic properties of PtSe₂ monolayer through transition metal doping J. Phys.: Condens. Matter 31 145502
- [13] Li P, Li L and Zeng X C 2016 Tuning the electronic properties of monolayer and bilayer PtSe₂ via strain engineering *J. Mater. Chem.* C 4 3106–12
- [14] Guo S-D 2016 Biaxial strain tuned thermoelectric properties in monolayer PtSe₂ J. Mater. Chem. C 4 9366–74
- [15] Yim C et al 2016 High-performance hybrid electronic devices from layered PtSe₂ films grown at low temperature ACS Nano 10 9550–8
- [16] Sajjad M, Montes E, Singh N and Schwingenschlögl U 2017 Superior gas sensing properties of monolayer PtSe₂ Adv. Mater. Interfaces 4 2–5
- [17] Yu X et al 2018 Atomically thin noble metal dichalcogenide: a broadband mid-infrared semiconductor Nat. Commun. 9 1545
- [18] Yan M et al 2017 High quality atomically thin PtSe₂ films grown by molecular beam epitaxy 2D Mater. 4 045015
- [19] Wang Z, Li Q, Besenbacher F and Dong M 2016 Facile synthesis of single crystal PtSe₂ nanosheets for nanoscale electronics Adv. Mater. 28 10224–9
- [20] Xie J et al 2019 Optical properties of chemical vapor deposition-grown PtSe₂ characterized by spectroscopic ellipsometry 2D Mater. 6 035011
- [21] Han S S et al 2019 Horizontal-to-vertical transition of 2D layer orientation in low-temperature chemical vapor deposition-grown PtSe₂ and its influences on electrical properties and device applications ACS Appl. Mater. Interfaces 11 13598–607
- [22] Xu H et al 2019 Controlled doping of wafer-scale PtSe₂ films for device application Adv. Funct. Mater. 29 1805614
- [23] Su T Y, Medina H, Chen Y Z, Wang S W, Lee S S, Shih Y C, Chen C-W, Kuo H-C, Chuang F-C and Chueh Y-L 2018 Phase-engineered PtSe₂-layered films by a plasma-assisted selenization process toward all PtSe₂-based field effect transistor to highly sensitive, flexible, and wide-spectrum photoresponse photodetectors *Small* 14 1–10
- [24] O'Brien M *et al* 2016 Raman characterization of platinum diselenide thin films *2D Mater.* **3** 021004
- [25] Xie C, Zeng L, Zhang Z, Tsang Y H, Luo L and Lee J H 2018 High-performance broadband heterojunction photodetectors based on multilayered PtSe₂ directly grown on a Si substrate *Nanoscale* 10 15285–93
- [26] Yuan J et al 2018 Wafer-scale fabrication of two-dimensional PtS2/PtSe₂ heterojunctions for efficient and broad band photodetection ACS Appl. Mater. Interfaces 10 40614–22
- [27] Ansari L et al 2019 Quantum confinement-induced semimetal-to-semiconductor evolution in large-area

2D Mater. **9** (2022) 025029 M Hilse et al

- ultra-thin PtSe₂ films grown at 400 °C npj 2D Mater. Appl. 3 33
- [28] Li L et al 2018 Wafer-scale fabrication of recessed-channel PtSe₂ MOSFETs with low contact resistance and improved gate control IEEE Trans. Electron Devices 65 4102–8
- [29] Jiang W *et al* 2019 Large-area high quality PtSe₂ thin film with versatile polarity *InfoMat* 1 260–7
- [30] Yim C, Passi V, Lemme M C, Duesberg G S, Ó Coileáin C, Pallecchi E, Fadil D and McEvoy N 2018 Electrical devices from top-down structured platinum diselenide films npj 2D Mater. Appl. 2 5
- [31] Ugeda M M et al 2014 Giant bandgap renormalization and excitonic effects in a monolayer transition metal dichalcogenide semiconductor Nat. Mater. 13 1091–5
- [32] Jia T, Rebec S N, Tang S, Xu K, Sohail H M, Hashimoto M, Lu D, Moore R G and Shen Z-X 2018 Epitaxial growth of TiSe 2 /TiO 2 heterostructure 2D Mater. 6 011008
- [33] Yue R et al 2015 HfSe₂ thin films: 2D transition metal dichalcogenides grown by molecular beam epitaxy ACS Nano 9 474–80
- [34] Liu H J, Jiao L, Xie L, Yang F, Chen J L, Ho W K, Gao C L, Jia J F, Cui X D and Xie M H 2015 Molecular-beam epitaxy of monolayer and bilayer WSe₂: a scanning tunneling microscopy/spectroscopy study and deduction of exciton binding energy 2D Mater. 2 034004

- [35] Liang L, Zhang J, Sumpter B G, Tan Q, Tan P and Meunier V 2017 Low-frequency shear and layer-breathing modes in Raman scattering of two-dimensional materials ACS Nano 11 11777–802
- [36] Zhang X, Qiao X, Shi W, Wu J, Jiang D and Tan P 2015 Phonon and Raman scattering of two-dimensional transition metal dichalcogenides from monolayer, multilayer to bulk material *Chem. Soc. Rev.* 44 2757–85
- [37] Xiong K, Hilse M, Li L, Goritz A, Lisker M, Wietstruck M, Kaynak M, Engel-Herbert R, Madjar A and Hwang J C M 2020 Large-scale fabrication of submicrometer-gate-length MOSFETs with a trilayer PtSe₂ channel grown by molecular beam epitaxy *IEEE Trans. Electron Devices* 67 796–801
- [38] Tuschel D 2016 Photoluminescence spectroscopy using a Raman spectrometer *Spectroscopy* **31** 14–21
- [39] Kandemir A, Akbali B, Kahraman Z, Badalov S V, Ozcan M, Iyikanat F and Sahin H 2018 Structural, electronic and phononic properties of PtSe₂: from monolayer to bulk Semicond. Sci. Technol. 33 085002
- [40] Tuschel D 2017 Why are the Raman spectra of crystalline and amorphous solids different? Spectroscopy 32 26–33
- [41] Hilse M, Wang K and Engel-Herbert R 2020 Growth of ultrathin Pt layers and selenization into PtSe₂ by molecular beam epitaxy 2D Mater. 7 11–14